Full length article

Electronic structure, phase formation, and defect distribution in the Ba(Ce,Fe,Acc)O$_{3-\delta}$ system

R. Merkle [a,*] [ORCID], M.F. Hoedl [a] [ORCID], A. Chesnokov [b] [ORCID], D. Gryaznov [b] [ORCID], E. Bucher [c] [ORCID], E.A. Kotomin [a,b] [ORCID], W. Sitte [c] [ORCID], J. Maier [a] [ORCID]

[a] Max Planck Institute for Solid State Research, Stuttgart, Germany
[b] Institute of Solid State Physics, University of Latvia, Riga, Latvia
[c] Chair of Physical Chemistry, Montanuniversitaet Leoben, Leoben, Austria

ARTICLE INFO

ABSTRACT

Composites of two perovskites are one possibility to combine protonic and p-type electronic conductivity as required for oxygen electrodes in protonic ceramic electrochemical cells. The BaCeO$_3$-BaFeO$_3$ system can be acceptor-doped to increase proton uptake and transport. However, preceding experiments [C. Berger et al., J. Mater. Chem. A 10 (2022) 2474; C. Nader et al., Solid State Ionics 406 (2024) 116474] indicated that the dopants are inhomogeneously distributed between the two phases, which is decisive for hydration ability and proton conductivity of such composites. Here, we use extended density functional theory calculations (DFT+U, Hubbard approach) for a comprehensive characterization of the BaCeO$_3$-BaFeO$_3$ system including acceptors. Supercells of various compositions are calculated to derive chemical reaction energies, for example for the transfer of defects between the phases. Two key aspects related to the hydration ability of such materials are: (i) The development of the electronic structure with increasing Fe content in a (hypothetical) single-phase BaCe$_{1-x}$Fe$_x$O$_3$ perovskite. (ii) The distribution of acceptors (Ga^{3+}, Sc^{3+}, In^{3+}, Y^{3+}) and oxygen vacancies (V$_O^{\bullet\bullet}$) between Ce- and Fe-rich phases. The segregation driving forces of acceptor dopant and V$_O^{\bullet\bullet}$ are calculated individually. V$_O^{\bullet\bullet}$ have the largest driving force towards the Fe-rich phase; ion radii and acid/base properties of the different acceptor dopants play a secondary role. The co-segregation of acceptors and V$_O^{\bullet\bullet}$ into the ferrate phase unfortunately decreases the hydration ability of the Ce-rich proton conductor phase. Analogous trends are expected for related proton- and hole-conductor perovskite composites, which partially counteracts the intended mixed conductivity.

1. Introduction

Protonic ceramic electrochemical cells have the potential to play an important role in the conversion and storage of fluctuating renewable energies, in particular because in electrolysis mode they allow for direct production of dry, compressed hydrogen (see e.g. [1–5]). The kinetics at the oxygen electrode (positrode) is key to the overall cell performance. For fast positrode kinetics, a high surface catalytic activity and good utilization of the available surface area of the porous electrode are required. This may be achieved with different positrode designs using either single-phase triple conducting oxides, or composites of materials which are mainly electron hole conductors with predominantly proton conducting materials (see e.g. [6–9]). For the latter, much activity was recently devoted to "self-organized" formation of composites from single precursor phases. Examples comprise mainly perovskite composites such as BaCeO$_3$-BaFeO$_3$ [10–12], and BaCeO$_3$-BaCoO$_3$ [13,14].

In the self-organized formation of composites, the spatial distribution of dopants and other point defects such as oxygen vacancies (V$_O^{\bullet\bullet}$) and protonic defects (OH$_O^{\bullet}$) among the developing phases is determined by thermodynamic driving forces as well as kinetics. Since cation diffusion in perovskites is much slower than proton or V$_O^{\bullet\bullet}$ diffusivity [15–18], it is not always clear whether the observed cation distribution actually represents thermodynamic equilibrium. As a result of the cation and defect distribution, a self-organized composite will actually consist of two phases which are both triple conductors - one close to an electrolyte-type composition but with increased electronic conductivity, and the other close to a typical positrode composition but with increased concentration of redox-inactive dopants. When composites of hole and proton conducting oxides are made by mixing separately prepared individual phases, generally a non-zero driving force for cation and defect

---

* Corresponding author.
   E-mail address: r.merkle@fkf.mpg.de (R. Merkle).

interdiffusion is expected. This may change material compositions during annealing/sintering (as part of device fabrication - typically few hours at temperatures above 800 °C), or during long-term device operation at lower temperatures.

In the present investigation we focus on the system $BaCeO_3$-$BaFeO_3$ as experimentally well-studied system. The actual cation distribution has a strong influence on the hydration properties of the phases. Over-sized dopants in $BaFeO_{3-\delta}$ perovskites have been shown to increase hydration, while already small concentrations of transition metal cations in protonic electrolyte materials such as $BaZrO_3$ strongly decrease hydration as found by thermogravimetry [6,19,20]. A similar effect is observed also for small amounts of iron dissolved in $BaCeO_3$ within the solubility range [21]. This motivates us to investigate the development of the electronic structure with increasing Fe content in the complete $BaCe_{1-x}Fe_xO_3$ solid solution series by density functional theory (DFT+U) calculations in Section 3.2 (note that experimentally in the middle of this series a miscibility gap appears). In the $BaZr_{1-x}Fe_xO_3$ system, the electronic density of states has been reported only for a few iron contents (4 %, 12 %, 25 %) [22].

The $BaCeO_3$-$BaFeO_3$ system exhibits a pronounced miscibility gap related to the lattice volume difference of 87.6 $Å^3$ vs. 65.7 $Å^3$ [10]. When doped with Y^{3+} or In^{3+} to increase proton uptake, this system shows distinct differences of dopant concentration between the two perovskite phases [11,23].

More insights into the relevant driving forces of defect redistribution between the phases are desired. In addition to ion size mismatch, other driving forces originating from acid-base properties and the specific electronic structure of the materials may play a role, and it is difficult to disentangle the contributions solely from experimental data. In Sections 3.5, we investigate the distribution of point defects in the Ba(Ce,Fe,Acc)$O_{3-\delta}$ system with Sc^{3+}, Y^{3+}, Ga^{3+} and In^{3+} as acceptors (denoted Acc' in Kröger-Vink notation, because these 3+ cations substituting for Ce^{4+} or Fe^{4+} are a defect with singly negative relative charge) using extended DFT+U calculations. The ionic radii of these dopants span a large range of 0.62–0.9 Å [24], and also differ in their chemical character: the Smith acidity values [25] are −1.6 for Ga_2O_3, −2.4 for In_2O_3 and −6.5 for Y_2O_3. For Sc_2O_3 a value of −5.9 can be estimated (adding the difference between Zr^{4+} (0.1) and Ti^{4+} (0.7) to the Y^{3+} value). In experimentally observed composites in the Ba(Ce,Fe,Acc)$O_{3-\delta}$ system the typical grain sizes are in the range of 50–200 nm, i.e. larger than the range for strong interfacial effects ("true size effects" [26]). Therefore, we concentrate here on bulk properties without considering space charge effects. While for undoped $BaFeO_3$ the hexagonal perovskite structure is the most stable polymorph [27], the experimentally applied acceptor doping stabilizes the cubic perovskite structure [6,23], thus we focus on this cubic structure also in the present DFT calculations.

2. Computational details

The DFT calculations are performed using the Vienna *ab initio* simulation package (VASP v.6.2.1 [28–30]) with the projector augmented wave (PAW) method [31] applying the Perdew–Burke–Ernzerhof (PBE) GGA-type functional [32] in combination with the rotationally invariant form of Hubbard U_{eff} correction [33] (U_{eff} = 4 eV for Fe, no U_{eff} for Ce f-states since Ce remains in formal 4+ oxidation state in all supercells) to treat strong electron correlation effects. We follow the methodology of our preceding work on $BaFeO_3$ [34, 35], with a plane wave energy cutoff of 500 eV and Brillouin zone sampling of the 5-atom primitive unit cell (space group $Pm\bar{3}m$) with a Γ-centered 8 × 8 × 8 Monkhorst–Pack k-point mesh [36]. The Monkhorst-Pack mesh was changed accordingly for the larger supercells with the number of atoms varied from 40 to 320. Fe is found to be always in high-spin state, all cells are calculated with ferromagnetic ordering. We use the total energy tolerances of 10^{-3} eV for the atomic structure and 10^{-6} eV for the electronic structure relaxations. Calculations are

performed for 40-atom (2 × 2 × 2) and occasionally also larger supercells with fully relaxed internal coordinates and lattice parameters (no symmetry restrictions, space group P1). The cation configurations are shown in Figs. S1 and S8. For $BaFeO_3$, a structure with Jahn-Teller-type distortion is found to have a lower energy than the undistorted cubic structure (by 0.02 eV/formula unit).

We note that, in contrast to $BaFeO_3$, the primitive unit cell of $BaCeO_3$ (orthorhombic phase, space group *Pnma*) actually comprises 4 formula units with lattice parameters of 6.23 × 6.25 × 8.79 Å [37]. In order to treat the entire $BaCeO_3$-$BaFeO_3$ system on an equal level, we use a 40-atom supercell with cell edge lengths of approximately 8.8 Å also for $BaCeO_3$. The obtained lattice parameters in Table S1 and the octahedra tilting pattern (Ce-O-Ce angle of 156°, Fig. S1) are sufficiently close to the experimental $BaCeO_3$ structure (Ce-O-Ce angles 157–160° [37], 157–158° [38]) to justify this approach.

For the calculation of the bulk modulus of $BaCeO_3$ and $BaFeO_3$ the cells are stretched or compressed isotropically to cover changes of supercell volume by up to ±15 % (optimizing all atom coordinates within the supercell); the modulus is determined from the third order Birch-Murnaghan equation [39,40]. For cells containing charged defects (a single 3+ acceptor, or a single doubly positively charged oxygen vacancy $V_O^{\bullet\bullet}$ in the supercell), a compensating background charge is applied. From these data we calculate the individual transfer energy of acceptors Acc' and of $V_O^{\bullet\bullet}$ from $BaCeO_3$ to $BaFeO_3$ via reaction (7,8) in Section 3.5.1. As a crosscheck - to demonstrate that potential size effects for charged cells do not significantly affect the respective energy differences - we calculate the transfer of (2 Acc' + $V_O^{\bullet\bullet}$) using only neutral cells as discussed in the supplementary information (SI, reaction (S1)), and also investigate the transfer of a $V_O^{\bullet\bullet}$ within neutral $Ba_{16}Ce_7Fe_7Y_2O_{47}$ cells which consist of a cerate- and a ferrate part. For the presentation of the electronic density of states (DOS) in Fig. 2, the oxygen states are separated into O connected only to Ce, only to Fe, or between Ce and Fe. Within these three groups there might still be slightly different oxygen atoms; then the DOS for one representative O is shown.

We write the chemical reaction equations using the composition of the respective supercells. For example, $Ba_8Ce_8O_{24}$ in Eq. (7) means a 40-atom cell containing 8 Ba, 8 Ce and 24 O atoms. Similarly, $Ba_8Ce_7AccO_{24}$ and $Ba_8Ce_8O_{23}$ in Eq. (7) mean cells which contain 8 Ba, 7 Ce one Y and 24 O atoms, and 8 Ba, 8 C, 23 O atoms and one oxygen vacancy (and a compensating background charge; as indicated in the text).

3. Results and discussion

3.1. Molar volume and bulk modulus

Before investigating the details of the electronic structure and energetics of point defects in the different phases, we calculate the bulk modulus of the defect-free $BaCeO_3$ and $BaFeO_3$ perovskites. The molar volumes of $BaCeO_3$ and $BaFeO_3$ differ strongly by 33 %, which leads to limited mutual solubility and a large miscibility gap. The bulk modulus is the relevant quantity to estimate the energetic contributions from compressive and tensile strain arising from the ion size mismatch in (hypothetical) $BaCe_{1-x}Fe_xO_3$ single-phase compositions as well as for acceptor dopants of different sizes in the cerate and ferrate phases.

The bulk moduli of the end members $BaCeO_3$ (109 GPa) and $BaFeO_3$ (95 GPa) are determined from isotropically strained supercells (Fig. 1a). The deviation of the latter value from literature DFT results [42] might be related to the fact that the $BaFeO_3$ bulk modulus in [42] was calculated in absence of a Jahn-Teller distortion (the presence of such a symmetry lowering often tends to decrease the bulk modulus, e.g. when comparing the cubic and non-cubic structures of $SrZrO_3$, $BaTiO_3$, $BaThO_3$). In a hypothetical $BaCe_{0.5}Fe_{0.5}O_3$ solid solution phase, integrating the strain energy relative to the relaxed $BaCeO_3$ and $BaFeO_3$ structures would result in an overall energy increase of ≈0.25 eV per
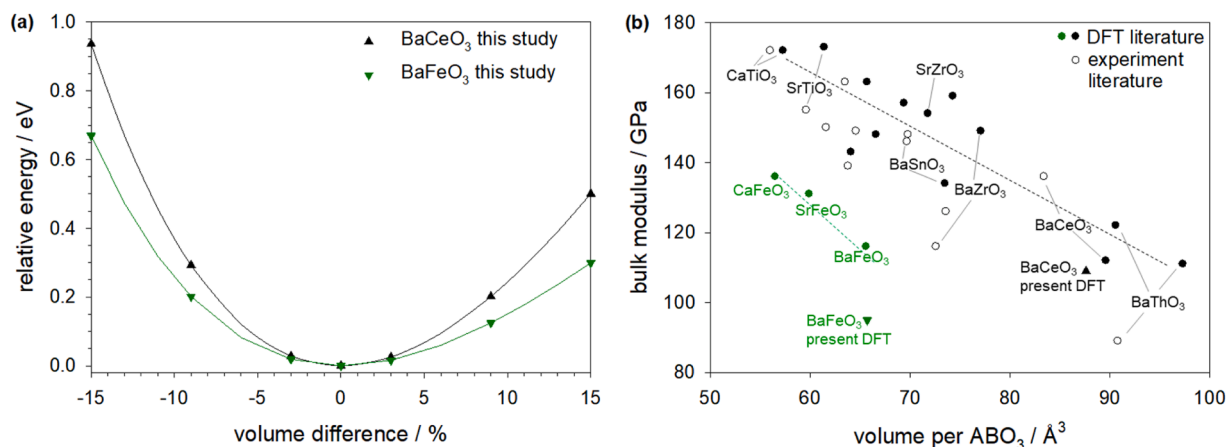
Fig. 1. (a) Relative energy of $BaCeO_3$ and $BaFeO_3$ (per formula unit) with isotropic strain from DFT, the lines represent the fit by the third order Birch-Murnaghan equation. (b) Bulk moduli of ABO_3 perovskites as function of cell volume. Open black circles: experimental data for $(Ca,Sr,Ba)(Ti,Zr,Ce,Hf,Th,Sn)O_3$ perovskites with large band gap, cf. [41] for list of materials and data sources. Solid black circles and dashed regression line: DFT calculations for the same perovskites with GGA functional [42]. Green circles: cubic phases of $CaFeO_3$, $SrFeO_3$, $BaFeO_3$ from [42] calculated with GGA+U, $U = 5.3$ eV Triangles: present calculations for $BaCeO_3$ (orthorhombic structure, DFT) and $BaFeO_3$ (tetragonal structure owing to Jahn-Teller distortion, DFT+U, $U = 4$ eV).

formula unit.

Fig. 1b compares experimental as well as DFT literature values for various $A^{2+}B^{4+}O_3$ perovskites. Within a materials family, the bulk modulus decreases with increasing molar volume. Interestingly, the bulk moduli of $(Ca,Sr,Ba)(Ti,Zr,Ce,Hf,Th,Sn)O_3$ are systematically higher than those of $(Ca,Sr,Ba)FeO_3$. The two groups differ in terms of their electronic structure, not only with respect to band gap (≥ 3 eV for $(Ca,Sr,Ba)(Ti,Zr,Ce,Hf,Th,Sn)O_3$, ≤ 0.6 eV or even (semi)metallic for $(Ca,Sr,Ba)FeO_3$) but also in the degree of covalency of the B-O bonds

(much higher for $(Ca,Sr,Ba)FeO_3$). This difference in bonding character might affect the elastic properties. However, other effects may also play a role ($La^{3+}(Fe,Co)^{3+}O_3$ perovskites with small bandgap follow the same trend line as large bandgap $A^{2+}B^{4+}O_3$ and $A^{3+}B^{3+}O_3$ perovskites).

3.2. Electronic density of states

Before analyzing the excess energies and miscibility gap in Sections 3.3-3.4 and the distribution of defects in Section 3.5, we first briefly
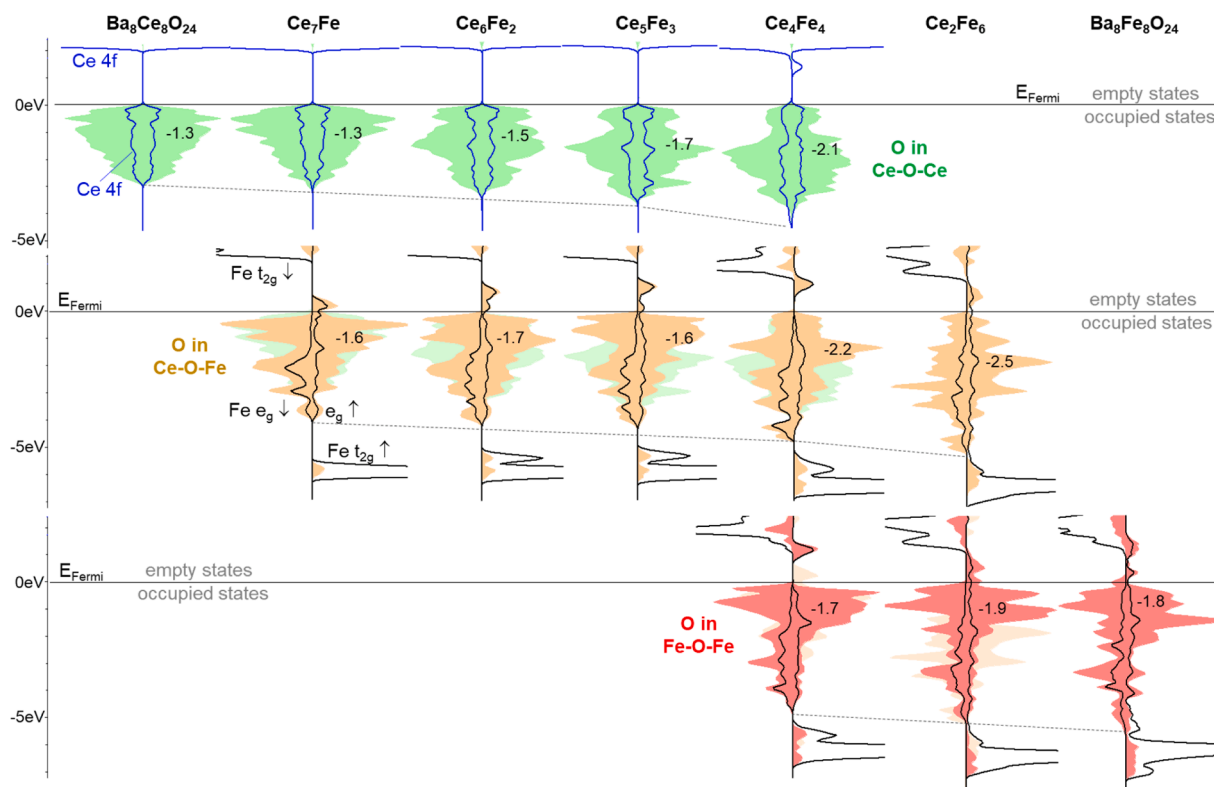
Fig. 2. Electronic DOS of (hypothetical) single-phase $BaCe_{1-x}Fe_xO_3$ for $0 \leq x \leq 1$. Partial DOS of O states shown as colored areas (but occupied only up to E_{Fermi}), Ce and Fe contribution as lines (the majority of Ce4f states as well as Fe3d spin down states lie above E_{Fermi} and are unoccupied). Top row: oxygen in Ce-O-Ce configurations, middle: Ce-O-Fe, bottom: Fe-O-Fe configurations. The numbers give the center-of-mass ε_O of the occupied O2p states relative to the Fermi level (in eV), the gray dashed lines emphasize the broadening of the O2p band width with increasing Fe content.

discuss the electronic density of states (DOS) of single-phase $BaCe_{1-x}Fe_xO_3$ perovskites. Experimentally, in absence of dopants the single-phase materials are metastable with respect to demixing for $0.15 \leq x \leq 0.85$ (cf. [10] and Section 3.4). However, the closely related $BaZr_{1-x}Fe_xO_3$ system [43], and the $BaCe_{1-x}Fe_xO_3$ system at high temperature in presence of Y dopants [11], form single-phase perovskite solid solutions. Thus it is reasonable and instructive to follow the gradual changes in the DOS of the hypothetical single-phase $BaCe_{1-x}Fe_xO_3$ perovskite. The solid solution members $Ba_8Ce_7FeO_{24}$ and $Ba_8CeFe_7O_{24}$ are close to the actual experimental phase boundaries [10, 11,23].

Fig. 2 shows the partial DOS of the oxygen states (O2p) and Ce4f, Fe3d states (Ba states are omitted for clarity). Corresponding to the high-spin state of iron, the spin-up Fe3d orbitals are largely occupied, while the spin-down Fe3d states are hardly occupied. This is best visible for the Fe t_{2g} states located ≈ 6 eV below and ≈ 2 eV above E_{Fermi}. The Fe e_g states are dispersed over an extended energy range, corresponding to partially covalent bonding with oxygen. A small admixture of Ce4f states is present in the valence band representing a slightly covalent character of the Ce-O bonds, but it is small compared to the main, unoccupied Ce4f DOS at 2–3.5 eV above E_{Fermi} (which is not fully displayed in Fig. 2). In $BaCeO_3$, the center-of-mass ε_O of the O2p states is located 1.3 eV below E_{Fermi}, and no unoccupied oxygen states are present above. Introducing one Fe in the supercell ($x = 0.125$) hardly affects oxygen atoms in Ce-O-Ce configurations, but for higher Fe content the shape of the oxygen DOS changes, the O2p band width increases, and ε_O moves downward. The DOS of oxygen in Ce-O-Fe shows distinctly more negative ε_O values relative to Ce-O-Ce already for the $Ba_8Ce_7FeO_{24}$ cell, which further increases for higher Fe content. O atoms connected to Fe exhibit unoccupied DOS above E_{Fermi}, which corresponds to holes in O2p states [6, 34]. The width of the O2p band broadens significantly from 3.1 eV in $BaCeO_3$ to 5.3–5.5 eV in Fe-rich compositions (Fig. S4a). This indicates an increasing degree of covalency of Fe-O but also Ce-O bonds with increasing Fe content. This is facilitated also by the decreasing lattice parameter; the dashed line in Fig S4a indicates that approx. half of the band width change originates from lattice parameter change. Most of the O2p band width increase occurs already for low Fe content, i.e. already for Ce-O-Fe bonds. The band width increase can also be related to the increased electronic conductivity, which is experimentally observed in the $BaZr_{1-x}Fe_xO_{3-\delta}$ and $BaZr_{0.88-x}Fe_xY_{0.12}O_{3-\delta}$ solid solutions already below $x \approx 0.2$, i.e. already before long-range uninterrupted Fe-O-Fe chains form [20,43].

While in Fig. 2 all DOS are aligned to a common Fermi level, DFT calculations for perovskite slabs in contact with vacuum show that the ionization potential (energy difference between top of valence band and vacuum level) is approximately 0.7 eV larger for $BaFeO_3$ compared to $BaCeO_3$ [6]. Thus, on an absolute energy scale, the lowering of the O2p center-of-mass is even more pronounced than shown in Fig. 2. Interestingly, the position of the Ba5p peak changes by a similar value of 0.9 eV from $BaCeO_3$ to $BaFeO_3$ (Table S1), thus one could tentatively use the difference of ε_O to this level as a proxy for the alignment on an absolute energy scale relative to vacuum as shown in Fig. S4d,f.

Such a lowering of the O2p center-of-mass is expected to affect the hydration thermodynamics of the respective materials: (i) for oxides with large bandgap, the proton affinity has been shown to correlate with the ionization potential - a smaller ionization potential corresponds to a more favorable proton affinity [44]. (ii) For $BaFeO_{3-\delta}$, the enthalpy of hydration was found to become more negative with increasing oxygen deficiency δ, i.e. with a higher position of the O2p states relative to the vacuum level [34]. Thus, the lowering of ε_O on an absolute energy scale (relative to vacuum) already for low Fe content (10–20 %) represents an important cause for the decreased hydration observed in Fe-doped $BaZrO_3$ and $BaCeO_3$ [11,20,23]. In the calculation of the averaged ε_O value for low Fe content, the number of Ce-O-Fe configurations increases with twice the slope than the Fe content itself (Fig. S4b), further aggravating this effect.

3.3. Energetics and local geometries in the $BaCe_{1-x}Fe_xO_3$ system

In this section we calculate the excess energy in the $BaFeO_3-BaCeO_3$ system. To keep the system well tractable, we concentrate on the situation in absence of additional defects (Acc', $V_O^{\bullet\bullet}$ or formation of Fe^{3+} species). Since the radius difference between Ce^{4+} and Fe is of comparable magnitude for both Fe oxidation states (0.285 Å for Fe^{4+}, and 0.225 Å for Fe^{3+}) the main cause for the nonideal mixing will not change too drastically in presence of oxygen deficiency. Fig. 3a shows the excess energy E_{xc} of $BaCe_{1-x}Fe_xO_3$ relative to the idealized interpolation between $BaCeO_3$ and $BaFeO_3$ as function of Fe fraction. For all intermediate compositions a positive excess energy is obtained.

$$E_{xc} = E(BaCe_{1-x}Fe_xO_3) - xE(BaFeO_3) - (1-x)E(BaCeO_3) \quad (1)$$

This is in line with the experimentally observed miscibility gap [10, 11,23]. The increase of E_{xc} is a bit steeper for Ce-rich materials than for Fe-rich compositions. This might be related to the following aspects: (i) The bulk modulus is lower for $BaFeO_3$, i.e. local strain from incorporating oversized Ce^{4+} is expected to cause less energy penalty. (ii) FeO_6 octahedra with Jahn-Teller distortion patterns may assist in the Ce^{4+} incorporation (cf. discussion below). The maximum excess energy of 0.13 eV in Fig. 3a is smaller than the estimated elastic excess energy of ≈ 0.25 eV (Section 3.1). Apparently the system experiences also energy gains for example from the intermixing of $BaFeO_3$ having a more acidic character with the more basic $BaCeO_3$.

The simplest model for nonideal behavior is the regular solution model [45] which assumes ideal entropy ($\Delta S_{xc}^0 = 0$) and describes the dependence of excess energy on the molar fraction x by a single interaction parameter Ω:

$$E_{xc} = \Omega x(1-x) \quad (2)$$

The E_{xc} data points obtained from the DFT calculations are used to fit the interaction parameter Ω of the system within the regular solution model according the Eq. (2). The dashed line in Fig. 3a represents the fit to Eq. (2), and yields an interaction energy $\Omega = 0.48$ eV/formula unit.

More complex models such as the Redlich-Kister model [46] would be able to reproduce the slight asymmetry in the calculated E_{xc}. In the thermodynamics theory of alloys also more complex approaches such as cluster expansion or concentration wave have been developed, see e.g. [47–50]. However, in order not to overfit the data, this would require the calculation of many more possible cation configurations, also in larger supercells. The goal of the present paper is to explore a materials system such as $BaCe_{1-x}Fe_xO_3$ with respect to different properties (geometrical structure, elastic properties, electronic structure, defect distribution), while a semiquantitative level with respect to individual numerical values suffices. Thus we model E_{xc} with the one-parameter phenomenological approach of Eq. (2). The authors are aware of the limitations of such mixture models for (partially) Coulombic systems, but their approximate validity is verified by the results which agree well with the experimental data.

Fig. 3b shows the variation of Ce-O and Fe-O distances in $BaCe_{1-x}Fe_xO_3$ with overall Fe fraction. The Ce-O distances decrease in an approximately linear mode with increasing Fe concentration. However, a close analysis of the structure shows that not only the Ce-O distances change but also the octahedral tilting that is typical for pure $BaCeO_3$ changes - it vanishes at $x \approx 0.4$. The situation for the Fe-O bonds is even more complex. $BaFeO_3$ exhibits a slight Jahn-Teller distortion (cf. [34, 51] for detailed discussion) and correspondingly a very broad distribution of Fe-O lengths. This holds also for Fe in the Ce-containing materials. For Fe-rich materials the oversized Ce^{4+} can be accommodated by local redistributions of the longer and shorter Fe-O bonds of the Jahn-Teller distortion without significantly expanding the average Fe-O distance. This effect might also explain the less steep E_{xc} increase for Fe-rich materials. Only for low iron contents $x \leq 0.375$ the average Fe-O length increases slightly. These observations indicate that the
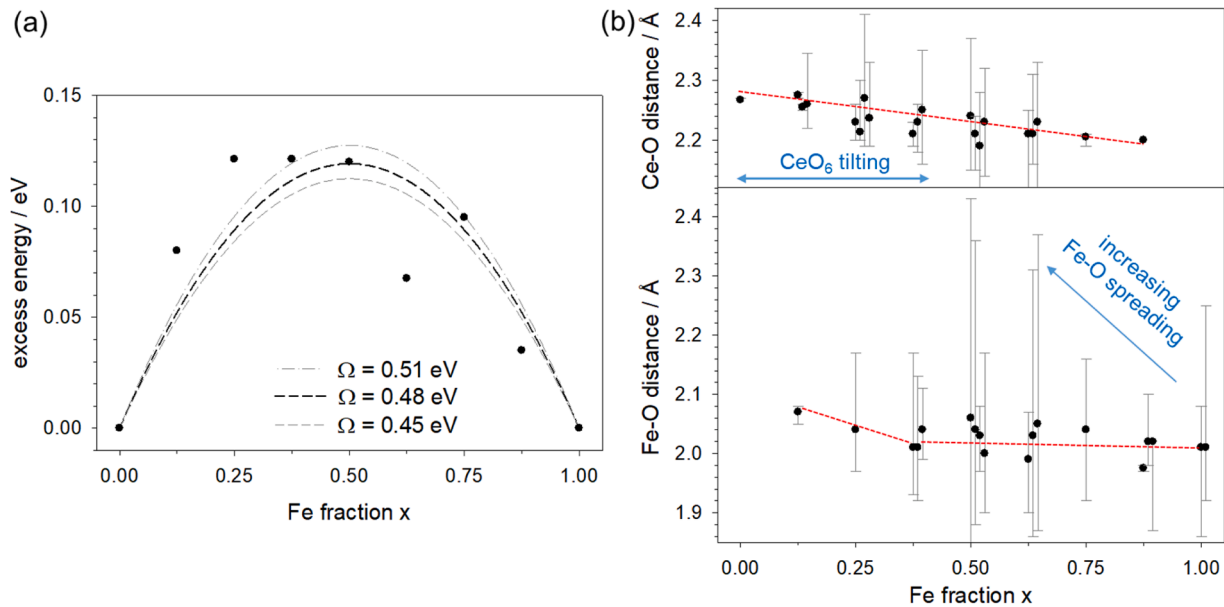
Fig. 3. (a) DFT excess energy E_{xc} (per ABO$_3$ formula unit) of single-phase BaCe$_{1-x}$Fe$_x$O$_3$. The black dashed line is a fit to Eq. (2) with an interaction parameter of Ω=0.48 eV (b) Ce-O and Fe-O distances in single-phase BaCe$_{1-x}$Fe$_x$O$_3$. The symbols show the average at respective atoms (with slight horizontal offset for better visibility), the error bars indicate the variation of Ce-O, Fe-O around the atom.

BaCe$_{1-x}$Fe$_x$O$_3$ system has more complex reasons for the deviation from an ideal solid solution than a simple ion size effect.

3.4. Miscibility gap

The miscibility gap in the BaFeO$_3$−BaCeO$_3$ system was calculated based on the interaction parameter $\Omega = 0.48$ eV (per ABO$_3$ formula unit) determined from the fitting to the DFT data points in Fig. 3a. Using the regular solution model, the free enthalpy of mixing can be obtained according to

$$\Delta G_{mix} = k_B\, T(x\ln x + (1-x)\ln(1-x)) + \Omega\, x\,(1-x) \tag{3}$$

where k_B is Boltzmann's constant, T the absolute temperature, x the Fe molar fraction. Fig. 4a shows ΔG_{mix} of the BaFeO$_3$−BaCeO$_3$ system as a function of the Fe molar fraction at different temperatures, from which the phase diagram of BaFeO$_3$−BaCeO$_3$ can be assessed, see Fig. 4b. At

high temperatures, miscibility is favored by the configurational entropy, whereas the system is expected to undergo phase separation with decreasing temperature. The binodal, i.e. the boundary below which phase separation would be thermodynamically favorable but possibly impeded by kinetic limitations, can be calculated according to

$$\frac{\partial \Delta G_{mix}}{\partial x} = k_B T(\ln x - \ln(1-x)) + \Omega\,(1-2x) = 0 \tag{4}$$

If the temperature decreases further, the spinodal is reached, i.e. the boundary below which the system will spontaneously separate into two phases, because there is no longer a kinetic hindrance. The spinodal can be obtained from the second derivative of ΔG_{mix} according to

$$\frac{\partial^2 \Delta G_{mix}}{\partial x^2} = k_B\, T\left(\frac{1}{x} + \frac{1}{1-x}\right) - 2\,\Omega = 0 \tag{5}$$

In their experimental study, Cheng et al. [10] found that (metastable) single phases in the BaFeO$_3$ −BaCeO$_3$ system occur when the Fe
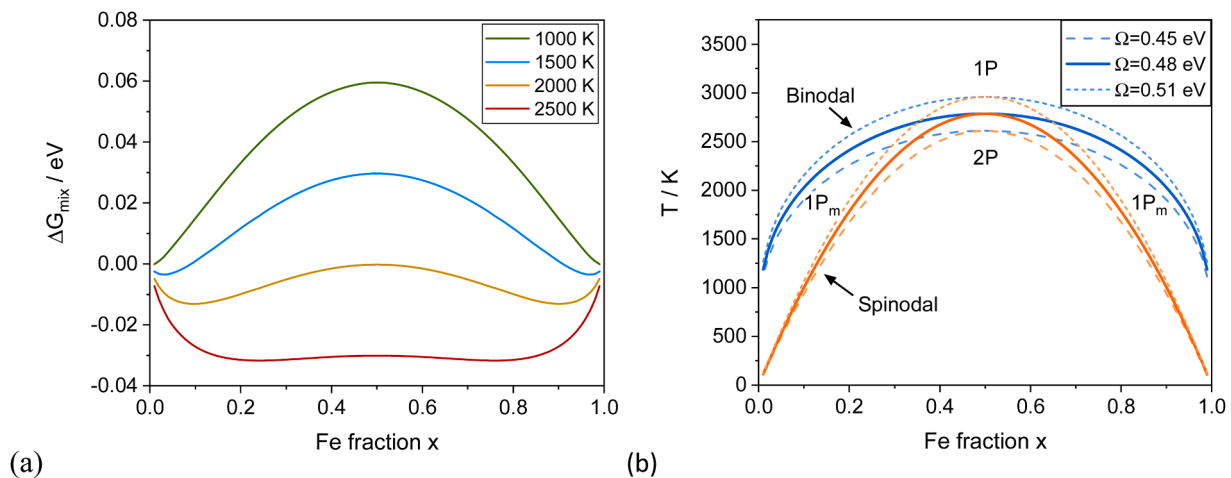
Fig. 4. (a) Free enthalpy of mixing (per ABO$_3$ formula unit) in the BaFeO$_3$−BaCeO$_3$ system as a function of Fe molar fraction x at different temperatures calculated with the regular solution model and $\Omega = 0.48$ eV (per ABO$_3$ formula unit). (b) Phase diagram with miscibility gap for the BaFeO$_3$−BaCeO$_3$ system showing the binodal and spinodal curves for $\Omega = 0.48 \pm 0.03$ eV. 1P denotes the single-phase region, 1P$_m$ the region where thermodynamics favors phase separation but kinetic limitations can lead to a metastable single phase, and 2P the region where spontaneous phase separation occurs.

content of samples sintered at 1643 K is < 0.15 or > 0.8. Taking the uncertainties in Ω into account, this is in good agreement with the spinodal curve obtained from the regular solution model in Fig. 4b.

The upper critical mixing temperature, which represents the intersection of the binodal and spinodal lines, is obtained at the maximum of the T vs. x curves according to

$$\left.\frac{\partial^2 \Delta G_{mix}}{\partial x^2}\right|_{x=0.5} = 0 \qquad (6)$$

at 2785 ± 174 K for $\Omega = 0.48 \pm 0.03$. This (theoretical) point predicted by the regular solution model is well above the melting temperature of the $BaFeO_3 - BaCeO_3$ system, which is observed around 1773 K. This result is also in line with the experimental study [10] which finds that the $BaFeO_3 - BaCeO_3$ system remains two-phase until melting occurs.

However, it should be emphasized that the phase diagram in Fig. 4b is to be interpreted with caution with respect to the following points: (i) The phase diagram is a theoretical approximation using the relatively simple regular solution model, predicting a symmetric miscibility gap. It is not a phase diagram determined experimentally by cooling from the melt, i.e. not via reversible separation/mixing. (ii) The interaction parameter Ω has been determined in Section 3.3 for the materials system without oxygen deficiency. (iii) The diagram does not take into account any further kinetic effects that are likely to occur in experimental studies involving finite time scales and relatively low temperatures.

While in the $BaFeO_3 - BaCeO_3$ system the large size mismatch between Ce^{4+} and Fe^{4+} leads to a large positive ΔG_{mix} even at typical sintering temperatures, the mismatch in $BaFeO_3 - BaZrO_3$ is smaller ($\Delta V/V \approx 12$ %) and owing to the steep nonlinear increase of relative energy with $\Delta V/V$ (Fig. 1a) the estimated elastic excess energy decreases to ≈ 0.06 eV Correspondingly, ΔG_{mix} becomes negative already at much lower temperatures, in agreement with the fact that experimentally a full solid solution is observed [43]. The perovskite structure is known to have a high ability for forming solid solutions with mixed occupancies on the A- and/or B-cation site. Many materials systems exhibit a moderate ion size mismatch, such that an ab initio thermodynamic analysis predicts a phase separation at temperatures below typical sintering conditions (e.g. [52–54]) but the very low cation diffusivities (see e.g. [15,16,17,18]) typically preserve the single-phase material.
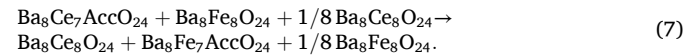
3.5. Distribution of point defects

3.5.1. Distribution of acceptors

Now we analyze the driving forces for the distribution of acceptors (and of $V_O^{\bullet\bullet}$ in Section 3.5.2) between the cerate and the ferrate in the 2-phase system. For the set of Ga^{3+}, Sc^{3+}, In^{3+}, Y^{3+} acceptors studied here, it is instructive to first analyze their size mismatch to the two host materials and its effect on bond lengths. Fig. 5 summarizes the Ce-O, Fe-O and Acc-O distances for $BaCeO_3$ and $BaFeO_3$ doped with 12.5 % of different acceptors Acc' (charge-compensated by a background charge). Relative to $BaCeO_3$, Ga, Sc and In are undersized, while Sc, In, Y are strongly oversized in $BaFeO_3$. The volume of the supercells varies systematically with dopant radius (Fig. S3), ranging from -1.3 % to $+1.4$ % in $BaCeO_3$ and up to $+5.5$ % in $BaFeO_3$. Fig. 5 shows that the average Ce-O distance remains constant, and also the Fe-O distance increases only very slightly. This means that the size mismatch of the dopants is accommodated rather by changes in the CeO_6 octahedra tilting in $BaCeO_3$, and reorientation of the Jahn-Teller distortion pattern in $BaFeO_3$, than by bond length modification. The unrelaxed size mismatch is of comparable magnitude for Ga^{3+} in $BaCeO_3$ and Y^{3+} in $BaFeO_3$ (dotted arrows in Fig. 5, estimated form the Shannon radii). However, in the relaxed geometry the Y-O length in $BaFeO_3$ is closer to the expected value than for Ga in $BaCeO_3$ (solid arrows in Fig. 5). The $BaFeO_3$ lattice is apparently softer (more tolerant) for size-mismatched dopants than $BaCeO_3$. This might also be related to its lower bulk modulus (sect. 3.1), and is also reflected in the slight asymmetry of the excess energy in Fig. 3a.

Using DFT calculations it is possible to analyze the driving forces for the distribution of Acc' and $V_O^{\bullet\bullet}$ (Section 3.5.2) between the cerate and ferrate phase separately. From the total energies of supercells without and with acceptor dopants, the reaction energy for a transfer of the dopant from the Ce-rich to the Fe-rich phase can be calculated according to

$$Ba_8Ce_7AccO_{24} + Ba_8Fe_8O_{24} + 1/8\,Ba_8Ce_8O_{24} \rightarrow$$
$$Ba_8Ce_8O_{24} + Ba_8Fe_7AccO_{24} + 1/8\,Ba_8Fe_8O_{24}. \qquad (7)$$

To be tractable in the DFT calculations, this reaction has to be expressed in terms of supercell compositions which comprise 8 formula units. The contributions such as $1/8\,Ba_8Ce_8O_{24}$ are needed to fill the B-site after removing the Acc' from a doped supercell. The cells which contain the Acc' acceptor are charge-compensated by a background charge, such that the transfer of the Acc' does not imply any change of Fe or Ce oxidation state. The same number of cells with background charge is present on both sides of reaction (7), thus any spurious effects of the background charge are expected to be of comparable magnitude for $Ba_8Fe_7AccO_{24}$ and $Ba_8Ce_7AccO_{24}$ cells and should cancel. As additional crosscheck, we also calculate the combined transfer of one $V_O^{\bullet\bullet}$ and two Acc' between neutral cells according to defect-chemical reaction (S1) in the SI (expanded cells containing 79 and 319 atoms. Table S2 demonstrates that the transfer energies for reaction (S1) between neutral cells
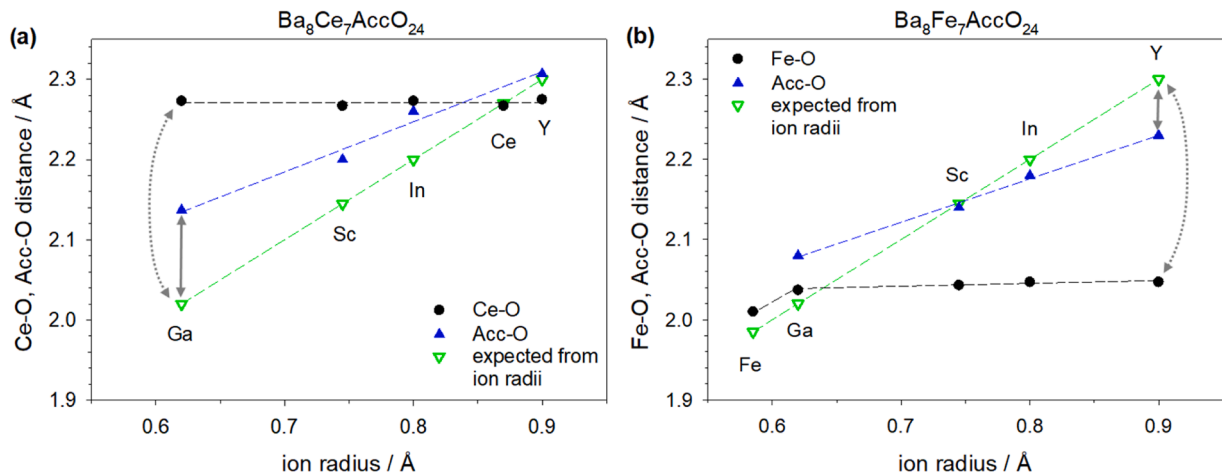

Fig. 5. Bond lengths for doped (a) $Ba_8Ce_7AccO_{24}$, and (b) $Ba_8Fe_7AccO_{24}$ as function of dopant radius. Solid circles: Ce-O and Fe-O averaged over entire cell, solid triangles: relaxed Acc-O distances, open triangles: M-O distances as expected from the Shannon radii.

are close to the respective sum of individual $V_O^{\bullet\bullet}$ and Acc^{3+} transfers between charged cells, supporting the validity of the individual transfer energies reported in Table 1.
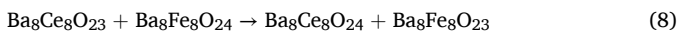
Since in a real material a range of local cation distributions and thus also energies occurs, the ΔE values in Table 1 should be considered as a relative ranking, rather than as precise numerical values. The largest overall driving force ΔE to segregate into the Fe-rich phase is found for Sc^{3+} (−0.48 eV) followed by Ga^{3+} (−0.37) and Y^{3+} (−0.27 eV), while In^{3+} has an almost vanishing driving force (+0.02 eV).

From a chemical point of view, we expect two main contributions to the dopant segregation energy, (i) elastic contributions from the size mismatch, (ii) contributions from the different acidity/basicity of the ions (empirically quantified by the Smith acidity [25]). Based on the set of Acc' and their properties (Table 1), it is possible to semi-quantitatively discuss their contributions to the total segregation energy obtained from reaction (7). Both contributions are expected to show nonlinear, over-proportional dependences on the difference between host and dopant. In first approximation the elastic energy is a parabolic function of local strain caused by dopant size mismatch. The Smith acidity parameter is related to the acid-base reaction energy in a quadratic manner similar to the Pauling definition of electronegativity [55]. Thus, the respective larger deviation of a dopant to either Ce^{4+} or Fe^{4+} is expected to dominate the overall elastic or acid-base energy contribution (indicated in boldface in Table 1).

Specifically, for Ga^{3+} the large size mismatch to Ce^{4+} dominates the elastic contribution, representing a driving force towards the Fe-rich phase. For Sc^{3+} the size mismatch is small relative to both Ce^{4+} and Fe^{4+}. For In^{3+} and Y^{3+} the mismatch to Fe^{4+} dominates, and constitutes a driving force towards the Ce-rich phase. All considered dopants exhibit the larger acidity difference to Fe^{4+}, which correspondingly dominates the acid-base contribution. All these contributions are summarized in Fig. 6. The overall driving force for Ga^{3+} is mainly given by the elastic contribution, while for Sc^{3+} it is largely determined by the acid-base interaction. The example of Y^{3+}, having a moderate overall driving force towards the Fe-rich phase despite large size mismatch with Fe^{4+}, emphasizes that also acid-base properties play an important role. For In^{3+}, elastic and acid-base contributions are small and have opposite direction such that In^{3+} should be distributed quite evenly. However, owing to the bulk electroneutrality conditions also the $V_O^{\bullet\bullet}$ distribution needs to be considered, as discussed in the next section.

3.5.2. Distribution of oxygen vacancies

In addition to acceptors, also oxygen vacancies may have a segregation driving force between the Ce-rich and the Fe-rich phase. The $V_O^{\bullet\bullet}$ segregation tendency is calculated from the reaction

$$Ba_8Ce_8O_{23} + Ba_8Fe_8O_{24} \rightarrow Ba_8Ce_8O_{24} + Ba_8Fe_8O_{23} \qquad (8)$$

To avoid changes of the cation valence (i.e. to extract the energy for

oxygen vacancy redistribution without involving additional redox processes), the $Ba_8Ce_8O_{23}$ and $Ba_8Fe_8O_{23}$ cells with one $V_O^{\bullet\bullet}$ are charge-compensated by a background charge. The energy of reaction (8) yields the driving force for the $V_O^{\bullet\bullet}$ transfer to the ferrate phase, which amounts to −1.58 eV. When this reaction energy is calculated using 79- and 80-atom and 319- and 320-atom supercells (bottom rows in table S1), it amounts to −1.55 eV and −1.21 eV. The fact that such a large cell expansion still yields a comparable reaction energy underpins that this strongly negative $V_O^{\bullet\bullet}$ segregation energy to the Fe-rich phase is not an artefact. We also performed additional crosschecks, based on $V_O^{\bullet\bullet}$ redistribution within neutral 80 atom $Ba_8(Ce,Fe)O_{23}$ cells containing both $V_O^{\bullet\bullet}$ and Acc^{3+} (fig. S8, table S3 in the SI). This yields a $V_O^{\bullet\bullet}$ segregation energy to the Fe-rich phase of 1.01–1.29 eV, which is in fair agreement with the range of 1.21–1.58 eV obtained from reaction (8) using different cell sizes.

The large negative reaction energy for reaction (8) means a large driving force for $V_O^{\bullet\bullet}$ to segregate to the Fe-rich phase, and it clearly exceeds the values obtained for the Acc' dopants in Table 1. Since in a real composite material local electroneutrality needs to be fulfilled, $V_O^{\bullet\bullet}$ and Acc' have to be transferred together to the macroscopic neighboring phase, and the larger share of the overall driving force stems from $V_O^{\bullet\bullet}$.

It is important to note that reaction (8) does not involve valence changes of Fe or Ce, i.e. the segregation tendency of $V_O^{\bullet\bullet}$ to $BaFeO_3$ is not caused by the chemically more facile reduction $Fe^{4+} \rightarrow Fe^{3+}$ compared to $Ce^{4+} \rightarrow Ce^{3+}$. Some insight into the $V_O^{\bullet\bullet}$ segregation energy is obtained from analyzing the structural changes. $V_O^{\bullet\bullet}$ introduction decreases the cell volume of $BaCeO_3$ by 3 % and of $BaFeO_3$ by 5 % (the fact that the volume decreases agrees with [56] that a $V_O^{\bullet\bullet}$, when not accompanied by reduction of a cation, has a smaller effective radius than an oxide ion). Even stronger differences are seen in local bond lengths. In $BaCeO_3$ the remaining Ce-O bonds at the Ce with the $V_O^{\bullet\bullet}$ in the first coordination shell contract by 4 % (0.09 Å). In contrast, a much stronger Fe-O contraction at five-fold coordinated Fe appears in $BaFeO_3$, it reaches 8 % (0.15 Å). This indicates that $BaFeO_3$ has a higher ability to compensate the absence of one oxide ion by strengthening the remaining Fe-O bonds, which can be attributed to a more covalent character of Fe-O bonds compared to Ce-O (cf. also the least favorable proton affinity of an O opposite to a $V_O^{\bullet\bullet}$ in $BaFeO_{3-\delta}$ [35]).

The Acc' segregation energy is calculated in Section 3.5.1 for materials compositions in which iron is always in the formal 4+ oxidation state. Introducing Fe^{3+} together with the respective oxygen deficiency might lead to some smaller changes of the Acc' segregation energy. However, the $V_O^{\bullet\bullet}$ segregation energy of −1.5 eV is much larger than the Acc' segregation energies and the Acc' distribution is largely coupled to the $V_O^{\bullet\bullet}$ distribution by the electroneutrality condition. Therefore we consider it reasonable to analyze the defect distribution based on fully oxidized materials compositions.

3.5.3. Effect of acceptor-oxygen vacancy association

In addition to the individual driving forces for Acc' and $V_O^{\bullet\bullet}$ segregation, interaction between these defects might further modify the segregation driving force. Related perovskites such as $BaZr_{1-x}Y_xO_{3-x/2}$ exhibit an attractive interaction between these defects. An $V_O^{\bullet\bullet}$ in the first and second coordination sphere of Acc' is lower in energy compared to large separation by approx. 0.4 eV (interaction with only one Y^{3+} [57]), or by up to 1.4 eV (interaction with two Y^{3+} which are located at 4.2 Å distance [41]). Exemplary Y^{3+}-$V_O^{\bullet\bullet}$ interactions in $BaCeO_3$ and $BaFeO_3$ are explored in Table S4. In the cerate, the interaction energies with a single Y^{3+} remain below 0.2 eV, the most stable $V_O^{\bullet\bullet}$ position is in the first sphere around Y^{3+}. For the ferrate the most stable position is in the second sphere, with strong repulsion in the first sphere and a moderate interaction energy < 0.2 eV relative to large distances. A comparable range of interaction energies is expected also for the other Acc^{3+} in $BaCeO_3$ and $BaFeO_3$, with some variation depending on the specific combination of dopant and host. For the distribution of Acc' and $V_O^{\bullet\bullet}$

Table 1
Energies ΔE for Acc' transfer from $BaCeO_3$ to $BaFeO_3$ phase according to Eq. (7), and related properties.* The dominating contributions of size mismatch Δr and Smith acidity [25] difference to Ce^{4+}/Fe^{4+} are indicated in boldface (see discussion in text).

Acc'	ΔE for reaction (7) / eV	radius for CN=6 / Å	Δr to Ce^{4+} / Å	Δr to Fe^{4+} / Å	Smith acidity of Acc_2O_3	diff. to Ce^{4+}	diff. to Fe^{4+}
Ga^{3+}	−0.37	0.62	**−0.25**	−0.035	−1.6	+1.1	**−1.9**
Sc^{3+}	−0.48	0.745	−0.125	+0.16	−5.9	−3.2	**−6.2**
In^{3+}	+0.02	0.8	−0.07	**+0.215**	−2.4	+0.3	**−2.7**
Y^{3+}	−0.27	0.9	+0.03	**+0.315**	−6.5	−3.8	**−6.8**

* Ionic radii [24] of Ce^{4+} / Fe^{4+} are 0.87 / 0.585 Å, Smith acidity [25] for CeO_2 and "FeO_2" (i.e. Fe^{4+}) are −2.7 / ≈0.3 (the acidity of Fe^{4+} is estimated extrapolating from FeO via Fe_2O_3 to FeO_2 and comparing to TiO_2). Less negative Smith acidity values mean higher acidity.
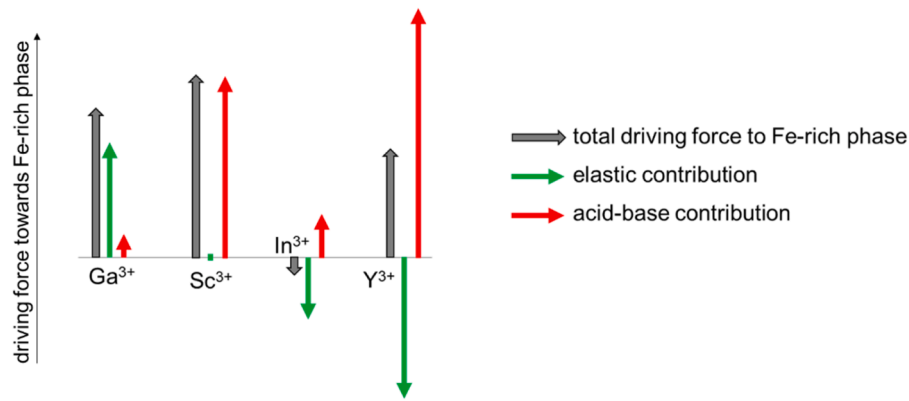
Fig. 6. Semiquantitative plot of the contributions of size mismatch (green arrows) and acid-base interactions (red) to the overall Acc' segregation driving force towards the Fe-rich phase (gray arrows, representing the ΔE values from Table 1).

between the ferrate and cerate phases, only the differences in the Acc'-$V_O^{\bullet\bullet}$ interaction energy would contribute (which is a second order effect). $V_O^{\bullet\bullet}$ would move from the low-energy position in the first and/or second sphere around the Acc' in the cerate phase to a similar position (with comparable Acc'-$V_O^{\bullet\bullet}$ interaction energy) around an Acc' in the ferrate. When Acc' co-segregate with $V_O^{\bullet\bullet}$ into the ferrate, they are also expected to find a similar low-energy position as they had in the cerate. A more detailed screening of these interaction energies is beyond the scope of the present investigation. As long as extremely strong differences in the interaction energy of a given Acc' with $V_O^{\bullet\bullet}$ in the cerate and ferrate phase are absent, the qualitative sequence of the segregation driving forces (Fig. 6) should remain unchanged.

3.6. Discussion and comparison with experiments

In this section the results from the DFT calculations are compared with the experimental observations. The first aspect is the miscibility gap. Experimentally, in absence of acceptor dopants the BaCeO₃-BaFeO₃ system shows a miscibility gap up to the melting temperature, with approx. 15 % mutual solubility at both edges [10]. This is in good agreement with the prediction in Fig. 4. Introducing 20 % of oversized Y^{3+} dopants increases the miscibility such that the gap vanishes above 1400 °C [11]. For the less oversized In^{3+}, the mutual solubility at elevated temperature is larger than for the undoped BaCeO₃-BaFeO₃, but some gap remains [23]. Qualitatively, the increased miscibility with oversized acceptors can be explained by the fact that the dissolution of these dopants in the Fe-rich phase expands its lattice parameter. Correspondingly, the size mismatch to BaCeO₃ and the miscibility gap decreases.

The main DFT result concerning the point defect distribution is that the driving force for $V_O^{\bullet\bullet}$ segregation to the Fe-rich phase is much larger than the respective contributions from various Acc'. Thus, strong accumulation of Acc' and $V_O^{\bullet\bullet}$ in the Fe-rich phase is expected for all considered acceptors despite their quite different acidity and size mismatch. Local dopant distributions have been measured by STEM-EDX for Y^{3+}, In^{3+} and Sc^{3+} [11,23]. For composites with overall composition BaCe₀.₄Fe₀.₄Acc₀.₂O₃₋δ the ratio of acceptor concentration in the Fe-rich relative to the Ce-rich phase amounts to 2.7 (Y), 2 (In) and 2.9 (Sc), i.e. all acceptors are strongly accumulated in the Fe-rich phase and the relative magnitude follows the trend of the DFT calculations from Table 1 and Fig. 6.

While this overall agreement is good, one should keep in mind some additional factors in the experiments, which are not included in the present DFT modelling. The dopant distribution occurs at high temperatures. The lattice parameters of both phases are expanded by thermochemical expansion (larger for BaFeO₃₋δ owing to increasing oxygen deficiency), but compared to the large lattice parameter differences

between BaCeO₃ and BaFeO₃ these effects are of minor importance.

Furthermore, the actual Fe-rich phase exhibits a pO_2- and T-dependent oxygen deficiency even in absence of acceptor doping. This may affect the defect distribution in two ways: (i) Partial reduction of Fe^{4+} to Fe^{3+} decreases the Smith acidity of the BaFeO₃ matrix (acidity −1.7 for Fe₂O₃, close to the Ga₂O₃ value). For Ga^{3+} this might even result in a (small) driving force towards the Ce-rich phase, but it is not expected to overcompensate the large tendency towards the Fe-rich phase caused by the size mismatch. For the other considered dopants the acidity difference to Fe remains larger than to Ce. (ii) A partial reduction of the ferrate phase is expected to decrease the degree of covalency of the Fe-O bonds, and thus may decrease the specific stabilization of $V_O^{\bullet\bullet}$ in the ferrate phase by strengthening the opposite Fe-O bond. (iii) The fact that already a high $V_O^{\bullet\bullet}$ concentration is present in the ferrate. This means that the gain of configurational entropy by further $V_O^{\bullet\bullet}$ segregation to the Fe-rich phase will be decreased. These aspects might lead to a smaller $V_O^{\bullet\bullet}$ and Acc' segregation tendency to the Fe-rich phase when the phase formation occurs under strongly reducing conditions, but it is not expected to vanish completely.

For the Acc^{3+} and $V_O^{\bullet\bullet}$ segregation energies, the present investigation concentrated on a fixed defect concentration of 12.5 %. Thermogravimetric measurements of water uptake on BaCe₀.₆₋ₓFe₀.₄YₓO₃ ($0.1 \leq x \leq 0.3$) and BaCe₀.₆₋ₓFe₀.₄InₓO₃ ($0.2 \leq x \leq 0.3$) composites (Fig. 5a and SI Fig. 18a in [23]) show a monotonous increase of proton content with increasing acceptor concentration. This can be regarded as an indication that the dopant distribution between the phases does not exhibit any sudden changes with increasing defect concentration. The upper limit of acceptor concentration is given either by the solubility limit (often ≈20 %), or for dopants with higher solubility by the fact that excessive substitution of Fe by redox-inactive dopants decreases the electronic conductivity too much.

While the present investigation focused on the BaCeO₃-BaFeO₃ system, the conclusions regarding Acc' and $V_O^{\bullet\bullet}$ distribution should apply to a broader range of electrolyte-type and triple-conducting perovskites phases. The Acc' segregation energies can be roughly estimated from size mismatch and acidity difference of the Acc' to the B-site cation of the triple conductor, which is typically more acidic than the B-cation of the electrolyte material. Also for materials other than BaFeO₃ a large driving force for $V_O^{\bullet\bullet}$ towards the triple conducting perovskite is expected, because with late transition metals as B-cation they have more covalent B-O bonds than typical electrolyte perovskites and can better stabilize the presence of an oxygen vacancy. Thus, the Acc' and $V_O^{\bullet\bullet}$ accumulation in the triple conducting perovskite and corresponding Acc', $V_O^{\bullet\bullet}$ depletion in the electrolyte, which is detrimental for its hydration and proton conductivity, is most probably a general phenomenon of such composites.

4. Conclusions

The present investigation shows that already from a limited number of supercell calculations important qualitative and semiquantitative insights into a complex two-phase system and the respective defect distributions can be obtained. For the BaCeO$_3$-BaFeO$_3$ system the miscibility gap is well reproduced. The calculated electronic density of states illustrates how even low Fe contents strongly affect the properties of a BaCeO$_3$ matrix. The lowering of the O2p state center-of-mass is expected to play a significant role in the decreasing degree of hydration already for moderate Fe concentration.

The spatial distribution of Acc' and V$_O^{\bullet\bullet}$ defects between the Ce-rich and Fe-rich phases can be calculated separately, demonstrating that the driving force for V$_O^{\bullet\bullet}$ dominates and thus all considered Acc' have a segregation tendency towards the Fe-rich phase (despite different acidity and size mismatch). The pronounced Acc' and V$_O^{\bullet\bullet}$ accumulation in the ferrate perovskite phase strongly decreases the hydration ability of the cerate phase. Thus it partially undermines the intended effect of combining a mainly proton-conducting and a mainly electronic/V$_O^{\bullet\bullet}$ conducting phase in a self-generated perovskite-perovskite composite. As alternative approach it might be worth to explore composite systems in which the two phases have a more different structure and/or defect chemistry to better preserve the separate properties of the involved phases.

CRediT authorship contribution statement

R. Merkle: Conceptualization, Methodology, Supervision, Writing – original draft, Writing – review & editing. **M.F. Hoedl:** Investigation, Writing – review & editing. **A. Chesnokov:** Investigation, Writing – review & editing. **D. Gryaznov:** Conceptualization, Methodology, Investigation, Supervision, Writing – original draft, Writing – review & editing, Funding acquisition. **E. Bucher:** Conceptualization, Methodology, Investigation, Writing – original draft, Writing – review & editing, Funding acquisition. **E.A. Kotomin:** Writing – review & editing, Funding acquisition. **W. Sitte:** Writing – review & editing. **J. Maier:** Writing – review & editing.

Declaration of competing interest

The authors declare that they have no known competing financial interests or personal relationships that could have appeared to influence the work reported in this paper.

Supplementary materials

Supplementary material associated with this article can be found, in the online version, at doi:10.1016/j.actamat.2025.120739.

References

[1] N.A. Danilov, I.A. Starostina, G.N. Starostin, A.V. Kasyanova, D.A. Medvedev, Z. P. Shao, Fundamental understanding and application of protonic Y- and Yb-codoped Ba(Ce,Zr)O$_3$ perovskites: state-of-the-art and perspectives, Adv. Energy Mater. 13 (2023) 2302175.

[2] C. Duan, R. Kee, H. Zhu, N. Sullivan, L. Zhu, L. Bian, D. Jennings, R. O'Hayre, Highly efficient protonic ceramic electrochemical cells for power generation and fuel production, Nature Energy 230 (2019) 230–240.

[3] S. Choi, T.C. Davenport, S.M. Haile, Protonic ceramic electrochemical cells for hydrogen production and electricity generation: exceptional reversibility, stability, and demonstrated faradaic efficiency, Energy Environ. Sci. 12 (2019) 206–215.

[4] E. Vøllestad, R. Strandbakke, M. Tarach, D. Catalán-Martínez, M.-L. Fontaine, D. Beeaff, D.R. Clark, J.M. Serra, T. Norby, Mixed proton and electron conducting double perovskite anodes for stable and efficient tubular proton ceramic electrolysers, Nature Mater. 18 (2019) 752–759.

[5] S. Guo, L. Jiang, Y. Li, P. Zhong, S.A. Ismail, T. Norby, D. Han, From electrolyte and electrode materials to large-area protonic ceramic fuel cells: a review, Adv. Funct. Mater. 34 (2024) 2304729.

[6] R. Merkle, M.F. Hoedl, G. Raimondi, R. Zohourian, J. Maier, Oxides with mixed protonic and electronic conductivity, Annu. Rev. Mater. Res. 51 (2021) 461–493.

[7] M. Papac, V. Stevanovic, A. Zakutayev, R. O'Hayre, Triple ionic-electronic conducting oxides for next-generation electrochemical devices, Nature Mater. 20 (2021) 301–313.

[8] J. Cao, Y. Jia, Z.P. Shao, Perovskites for protonic ceramic fuel cells: a review, Energy Environ. Sci. 15 (2022) 2200–2232.

[9] Q. Wang, S. Ricote, M. Chen, Oxygen electrodes for protonic ceramic cells, Electrochim. Acta 446 (2023) 142101.

[10] S. Cheng, Y. Wang, L. Zhuang, J. Xue, Y. Wei, A. Feldhoff, J. Caro, H. Wang, A dual-phase ceramic membrane with extremely high h$_2$ permeation flux prepared by autoseparation of a ceramic precursor, Angew. Chem. Int. Ed. 55 (2016) 10895–10898.

[11] C. Berger, E. Bucher, R. Merkle, C. Nader, J. Lammer, W. Grogger, J. Maier, W. Sitte, Influence of Y-substitution on phase composition and proton uptake of self-generated Ba(Ce,Fe)O$_{3-\delta}$-Ba(Fe,Ce)O$_{3-\delta}$ composites, J. Mater. Chem. A 10 (2022) 2474–2482.

[12] H. Tong, M. Fu, Y. Yang, F.L. Chen, Z. Tao, A novel self-assembled cobalt-free perovskite composite cathode with triple-conduction for intermediate proton-conducting solid oxide fuel cells, Adv. Funct. Mater. 32 (2022) 2209695.

[13] Y. Song, Y. Chen, W. Wang, C. Zhou, Y. Zhong, G. Yang, W. Zhou, M. Liu, Z.P. Shao, Self-Assembled triple-conducting nanocomposite as a superior protonic ceramic fuel cell cathode, Joule 3 (2019) 2842–2853.

[14] Z. Zhao, J. Cui, M. Zou, S. Mu, H. Huang, Y. Meng, K. He, K.S. Brinkman, J. Tong, Novel twin-perovskite nanocomposite cathode materials for protonic ceramic fuel cells, J. Power Src. 450 (2020) 227609.

[15] I. Hasle, S.P. Waldow, U.N. Gries, R.A. De Souza, E. Vollestad, R. Haugsrud, B-site cation inter-diffusion in yttrium substituted barium zirconate, J. Mater. Chem. A 9 (2021) 21142–21150.

[16] R. Sazinas, I. Sakaguchi, M.A. Einarsrud, T. Grande, ^{134}Ba diffusion in polycrystalline BaMO$_3$ (M = Ti, Zr, Ce), AIP Adv. 7 (2017) 115204.

[17] M. Kubicek, G.M. Rupp, S. Huber, A. Penn, A.K. Opitz, J. Bernardi, M. Stöger-Pollach, H. Hutter, J. Fleig, Cation diffusion in La$_{0.6}$Sr$_{0.4}$CoO$_{3-\delta}$ below 800 °C and its relevance for Sr segregation, Phys. Chem. Chem. Phys. 16 (2014) 2715–2726.

[18] S.P. Harvey, R.A. De Souza, M. Martin, Diffusion of La and Mn in Ba$_{0.5}$Sr$_{0.5}$Co$_{0.8}$Fe$_{0.2}$O$_{3-\delta}$ polycrystalline ceramics, Energy Environ. Sci. 5 (2012) 5803–5813.

[19] R. Zohourian, R. Merkle, G. Raimondi, J. Maier, Mixed-Conducting perovskites as cathode materials for protonic ceramic fuel cells: understanding the trends in proton uptake, Adv. Funct. Mater. 28 (2018) 1801241.

[20] G. Raimondi, R. Merkle, A. Longo, F. Giannici, O. Mathon, C.J. Sahle, J. Maier, Interplay of chemical, electronic and structural effects in the triple-conducting BaFeO$_3$ - Ba(Zr,Y)O$_3$ solid solution, Chem. Mater. 35 (2023) 8945–8957.

[21] C. Nader, R. Merkle, unpublished data.

[22] A. Marthinsen, G. Wahnstrom, Percolation transition in hole-conducting acceptor-doped barium zirconate, Chem. Mater. 32 (2020) 5558–5568.

[23] C. Nader, J. Lammer, A. Egger, C. Berger, W. Sitte, W. Grogger, R. Merkle, J. Maier, E. Bucher, Phase composition and proton uptake of acceptor-doped self-generated Ba(Ce,Fe)O$_{3-\delta}$ − Ba(Fe,Ce)O$_{3-\delta}$ composites, Solid State Ionics 406 (2024) 116474.

[24] R.D. Shannon, Revised effective ionic radii and systematic studies of interatomic distances in halides and chalcogenides, Acta Crystallogr. A 32 (1976) 751–767.

[25] D.W. Smith, An acidity scale for binary oxides, J. Chem. Educ. 64 (1987) 480–481.

[26] J. Maier, Nanoionics: ion transport and electrochemical storage in confined systems, Nature Mater 4 (2005) 805–815.

[27] S. Mori, Preparation of Various Phases of BaFeO$_{3-x}$, J. Am. Ceram. Soc. 48 (1965), 165-165.

[28] G. Kresse, J. Hafner, Ab-initio molecular dynamics for liquid metals, Phys. Rev. B: Condens. Matter Mater. Phys. 47 (1993) 558–561.

[29] G. Kresse, J. Furthmüller, Efficiency of ab-initio total energy calculations for metals and semiconductors using a plane-wave basis set, Comput. Mater. Sci. 6 (1996) 15–50.

[30] G. Kresse, J. Furthmüller, Efficient iterative schemes for ab-initio total-energy calculations using a plane-wave basis set, Phys. Rev. B: Condens. Matter Mater. Phys. 54 (1996) 11169–11186.

[31] P.E. Blöchl, Projector augmented-wave method, Phys. Rev. B: Condens. Matter Mater. Phys. 50 (1994) 17953–17979.

[32] J.P. Perdew, K. Burke, M. Ernzerhof, Generalized gradient approximation made simple, Phys. Rev. Lett. 77 (1996) 3865–3868.

[33] S. Dudarev, G. Botton, S. Savrasov, C. Humphreys, A. Sutton, Electron-energy-loss spectra and the structural stability of nickel oxide: an LSDA+U study, Phys. Rev. B 57 (1998) 1505–1509.

[34] M.F. Hoedl, D. Gryaznov, R. Merkle, E.A. Kotomin, J. Maier, Interdependence of oxygenation and hydration of mixed conducting (Ba,Sr)FeO$_{3-\delta}$ perovskites studied by density functional theory, J. Phys. Chem. C 124 (2020) 11780–11789.

[35] M.F. Hoedl, A. Chesnokov, D. Gryaznov, R. Merkle, E.A. Kotomin, J. Maier, Proton migration barriers in BaFeO$_{3-\delta}$ - insights from DFT calculations, J. Mater. Chem. A 11 (2023) 6336–6348.

[36] H.J. Monkhorst, J.D. Pack, Special points for Brillouin zone integrations, Phys. Rev. B 13 (1976) 5188–5192.

[37] K.S. Knight, Structural phase transitions in BaCeO$_3$, Solid State Ionics 74 (1994) 109–117.

[38] A.J. Jacobson, B.C. Tofield, B.E.F. Fender, The structures of BaCeO$_3$, BaPrO$_3$ and BaTbO$_3$ by neutron diffraction: lattice parameter relations and ionic radii in O-perovksites, Acta Cryst. B 28 (1972) 956–961.

[39] F.D. Murnaghan, Finite Deformations of an Elastic Solid, Am. J. Math. 59 (1937) 235–260.

[40] F. Birch, Finite elastic strain of cubic crystals, Phys. Rev. 71 (1947) 809–824.

[41] M.F. Hoedl, E. Makagon, I. Lubomirsky, R. Merkle, E.A. Kotomin, J. Maier, Impact of point defects on the elastic properties of BaZrO$_3$: comprehensive insight from experiments and ab initio calculations, Acta Mater. 160 (2018) 247e256.

[42] Data retrieved from Materials Project (https://legacy.materialsproject.org/), accessed in January 2024.

[43] D. Kim, S. Miyoshi, T. Tsuchiya, S. Yamaguchi, Percolation conductivity in BaZrO$_3$-BaFeO$_3$ solid solutions, Solid State Ionics 126 (2014) 875–878.

[44] T.S. Bjørheim, M.F. Hoedl, R. Merkle, E.A. Kotomin, J. Maier, Proton, hydroxide ion, and oxide ion affinities of closed-shell metal oxides: importance for the hydration reaction and correlation to electronic structure, J. Phys. Chem. C 124 (2020) 1277–1284.

[45] J.H. Hildebrandt, Solubility XII: regular solutions, J. Am. Ceram. Soc. 51 (1929) 66–80.

[46] O. Redlich, A.T. Kister, Thermodynamics of nonelectrolyte solutions - x-y-T relations in a binary system, Ind. Eng. Chem. 40 (1948) 345–348.

[47] J.W.D. Connolly, A.R. Williams, Density-functional theory applied to phase transformations in transition-metal alloys, Phys. Rev. B 27 (1983) 5169–5172.

[48] A.G. Khachaturyan, Theory of Structural Transformations in Solids, John Wiley & Sons, New York, 1983.

[49] J.M. Sanchez, Foundation and practical implementations of the cluster expansion, J. Phase Equilib. Diffus. 38 (2017) 238–251.

[50] P. Singh, A.V. Smirnov, A. Alam, D.D. Johnson, First-principles prediction of incipient order in arbitrary high-entropy alloys: exemplified in Ti$_{0.25}$CrFeNiAl$_x$, Acta Mater 189 (2020) 248–254.

[51] M.F. Hoedl, R. Merkle, R. Dronskowski, The orbital nature of electron holes in BaFeO$_3$ and implications for defect chemistry, J. Maier, J. Phys. Chem. C 126 (2022) 12809–12819.

[52] S. Piskunov, S. Dorfman, D. Fuks, E.A. Kotomin, Ba$_c$Sr$_{1-c}$TiO$_3$ perovskite solid solutions: thermodynamics from ab initio electronic structure calculations, Phys. Rev. B 71 (2005) 014111.

[53] A. Weizman, D. Fuks, E.A. Kotomin, D. Gryaznov, Ab initio study of phase competition in (La$_{1-c}$Sr$_c$)CoO$_3$ solid solutions, Solid State Ionics 230 (2013) 32–36.

[54] D. Fuks, Y. Mastrikov, E. Kotomin, J. Maier, Ab initio thermodynamic study of (Ba, Sr)(Co,Fe)O$_3$ perovskite solid solutions for fuel cell applications, J. Mater. Chem. A 1 (2013) 14320–14328.

[55] L. Pauling, The nature of the chemical bond, 3. ed. (1960).

[56] E. Jedvik, A. Lindman, M.P. Benediktsson, G. Wahnström, Size and shape of oxygen vacancies and protons in acceptor-doped barium zirconate, Solid State Ionics 275 (2015) 2–8.

[57] F.M. Draber, J.R. Denninger, P.C. Müller, I.K. Sommerfeld, M. Martin, The impact of nanoscale percolation in yttrium-doped BaZrO$_3$ on the oxygen ion and proton conductivities: a density functional theory and kinetic Monte Carlo study, Adv. Energy Sustain. Res. 3 (2022) 2200007.